

Hot-Electron Emission for Spectral Calibration

Leon Oleschko
Supervised by Peter Baum
09.08.2025
Universität Konstanz

Available at www.github.com/leoole100/projekt-praktikum.

1 Introduction

Accurate spectral measurements require knowledge of an instrument’s spectral response—how efficiently the system transmits and detects light as a function of wavelength. To recover physically meaningful spectra, the system response must be determined against a known reference and applied as a correction.

This work targets the ultraviolet (UV), where suitable calibration sources are limited. Deuterium lamps are the practical secondary standard in the UV (optionally combined with tungsten–halogen to bridge into the VIS–NIR), yet their spectral irradiance is sharply wavelength dependent and subject to aging and stability issues. In addition, they require periodic replacement and careful handling, which adds cost and maintenance burden to UV calibration workflows. Primary radiometric scales are realized using high-temperature graphite-cavity blackbodies operated near $\sim 3500\text{ K}$ and propagated via calibrated transfer standards to working instruments [1, 2].

As an alternative to a source-based procedure, a calibrated, near-flat detector can be used to establish a detector-based traceability chain; this approach has been demonstrated in practice and can substitute the lamp path in suitable setups [3].

Motivated by these constraints, we explore thermal radiation from hot electrons in solids as a broadband reference. Under ultrafast excitation, the electronic subsystem can reach effective temperatures of several thousand K on picosecond time scales [4], producing smooth, thermal-like emission that spans the UV–VIS. Because the spectrum is broadband, predictable from basic physics, and largely free from narrow spectral features, hot-electron emission offers one of the most straightforward routes to generating stable UV reference light—potentially replacing deuterium lamps where a compact, low-maintenance source is desirable. If stability, reproducibility, and an absolute radiometric scale can be established, hot-electron emission could offer a compact UV calibration route that competes with deuterium lamps while avoiding their spectral non-flatness.

2 Theory

To obtain the spectral shape, we model ultrafast absorption and subsequent thermal emission with a zero-dimensional (lumped) two-temperature picture for the probed volume. The probed volume is approximated as the excited spot area times the optical absorption depth, $V_{\text{probe}} \approx A_{\text{spot}} d_{\text{abs}}$. A short laser pulse deposits power $P(t)$ into the electronic system, which rapidly thermalizes; electron–phonon coupling then cools the electrons toward the lattice temperature T_l . Neglecting transport and other slow losses on the picosecond timescale, the electron temperature $T_e(t)$ obeys

$$\frac{dT_e}{dt} = -\frac{T_e - T_l}{g} + \frac{P(t)}{C_e(T_e)}. \quad (1)$$

Here $C_e(T_e)$ is the electronic heat capacity of the probed volume (units J/K), g is the electron–phonon energy-relaxation time, T_l is the lattice temperature (taken approximately constant over this window since typically $C_l \gg C_e$), and $P(t)$ is the laser power deposited in the

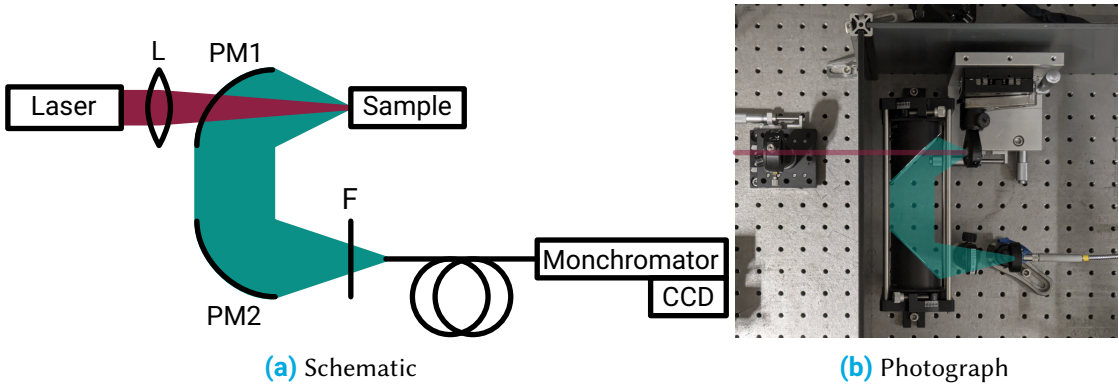


Figure 1 Experimental setup used to measure thermal emission from ultrafast-excited hot electrons. The schematic shows the optical path and key components; the photograph shows the arrangement inside the chamber.

probed volume (units W).

Because the instantaneous radiant exitance scales with T^4 (Stefan–Boltzmann law), the emission is dominated by the high-temperature portion of $T_e(t)$ immediately after excitation; the later, lower-temperature evolution contributes comparatively little. This justifies treating T_l as constant and using the simplified dynamics above when we are interested in the relative spectral shape rather than absolute irradiance.

To map $T_e(t)$ to the emitted spectrum we use Planck's law. The blackbody spectral radiance is

$$B(\lambda, T) = \frac{2hc^2}{\lambda^5} \frac{1}{\exp(\frac{hc}{\lambda k_B T}) - 1}. \quad (2)$$

Here B has the units $\text{W m}^{-2} \text{sr}^{-1} \text{nm}^{-1}$. The emissivity is assumed to be unity, as is commonly done for the material used here [2].

The quantity compared to the measurement is the spectral power density $P(\lambda)$ in W nm^{-1} . We obtain it from radiance by multiplying with the illuminated spot area A_{spot} and the collection solid angle Ω_{coll} (emission approximated as Lambertian within the collection cone) and integrating over the exposure window:

$$P(\lambda) = A_{\text{spot}} \Omega_{\text{coll}} \int B(\lambda, T_e(t)) dt. \quad (3)$$

3 Experimental Setup

The experimental setup, originally developed by Leon Roob [5], is shown in Figure 1. It is designed to measure broadband thermal emission from hot electrons in graphite using reflective collection optics and a fibre-coupled spectrometer.

The excitation source is a PHAROS PH1-20 (Light Conversion) at a centre wavelength of 1030 nm, with pulse duration 250 fs (FWHM) and repetition rate 40 kHz. The pulse energy

Parameter	Symbol	Value
Average laser power	P_{avg}	300(5) mW
Repetition rate	f_{rep}	40 kHz
Pulse duration	τ_{fwhm}	250(50) fs
Spot diameter on sample ¹	d_{spot}	70^{+50}_{-0} μm
Optical absorption depth	d_{abs}	200(100) nm [6]
Cooling time constant	g	250(50) fs [7]
Electronic heat capacity	$C_e(T_e)$	$\text{J m}^{-3}\text{K}^{-2}$ [8]
Lattice (ambient) temperature	T_l	300 K

Table 1 Model parameters used in the spectrum calculation. Uncertainties in 1σ .

is $7.5 \mu\text{J}$ (average power 300 mW). The beam is stabilised in four axes and expanded to a diameter of 5 mm before entering the chamber.

Inside the chamber, a plano-convex lens with focal length $f = 200$ mm focuses the beam onto the sample. Using the standard diffraction estimate $d \approx 4\lambda f/\pi D$ with $D = 5$ mm, the expected spot diameter is $\sim 50 \mu\text{m}$.

The target is a graphite sample mounted on a three-axis translation stage. Thermal emission from the irradiated spot is collected by two off-axis parabolic mirrors (UV-enhanced aluminium). The first mirror (PM1, $f = 50$ mm) collimates the emission; the second (PM2, $f = 101$ mm) focuses it onto a band-pass filter and into a multimode fibre with a $200 \mu\text{m}$ core (Ocean Optics QP200-2-SR-BX). The magnification is $M = f_{\text{PM2}}/f_{\text{PM1}} \approx 2$, yielding an image spot of $\sim 100 \mu\text{m}$ at the fibre entrance, comfortably within the core.

The fibre feeds an Acton SpectraPro 300i monochromator equipped with a $150 \text{ lines mm}^{-1}$ grating blazed at 500 nm. The dispersed spectrum is detected by an Andor iXon^{EM+} 897 EMCCD operated in vertical binning mode, effectively serving as a 1D line detector. Wavelength calibration (performed once following the manufacturer's procedure [5]) was stable throughout the measurements.

For alignment and maximal throughput, the lens, sample, and fibre ferrule are mounted on independent precision translation stages, while PM1 and PM2 are fixed on the common optical axis.

4 Methods

4.1 Model

We obtain the electron temperature trajectory $T_e(t)$ by numerically integrating the ODE in the Theory section (Equation 1), using a Gaussian pulse for $P(t)$ with per-pulse energy $E_p = P_{\text{avg}}/f_{\text{rep}}$. The time step Δt and integration window were chosen such that further refinement did not change the resulting spectrum appreciably. The parameters used are listed in Table 1.

The modeled spectral power density is then computed by inserting $T_e(t)$ into Planck's law (Equation 3) and integrating numerically over time.

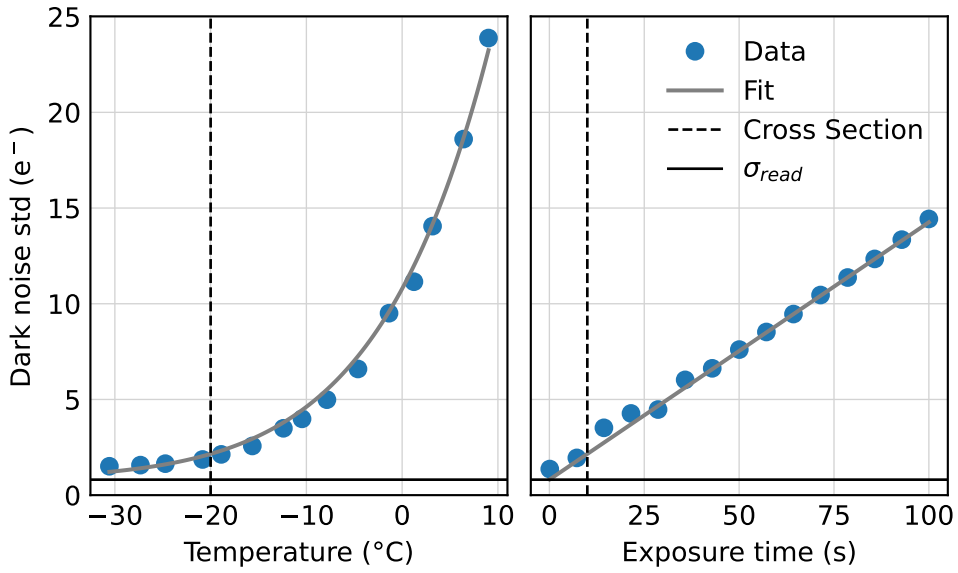


Figure 2 Dark noise vs. sensor temperature and exposure time. Fit yields $E = 0.597(4)$ eV and $\sigma_{\text{read}} = 0.81(12)$ e⁻.

To estimate uncertainties, we sample the parameters in Table 1 within their stated 1σ ranges, recompute the spectrum for each draw, and report, for each wavelength, the mean and standard deviation.

4.2 Noise and detector considerations

Detecting the weak thermal radiation from hot electrons requires careful optimisation of the signal-to-noise ratio (SNR). In this setup the dominant noise sources originate from the detector; laser power fluctuations are treated as negligible. The EMCCD mechanisms are well documented by Andor [9, 10] and standards [11].

Readout noise. This is the fundamental noise from charge transfer and A/D conversion. For the present camera, the fit in Figure 2 yields a constant read noise of $\sigma_{\text{read}} = 0.81(12)$ e⁻, consistent with the manufacturer's specification [12]. Because read noise is applied per read out bin, hardware binning (1D line-detector mode) reduces its impact by summing signal prior to the single read.

Dark current noise. Thermally generated charge scales with temperature and time, $N_{\text{dark}} \propto \exp(-E/kT) t_{\text{exp}}$. Figure 2 shows the measured dependence; fitting gives an effective activation energy $E = 0.597(4)$ eV. With the sensor cooled to -80 °C, the dark contribution is negligible at the exposure times used.

Clock-induced charge (CIC). CIC is created during high-speed clocking. Its apparent contribution grows with electron multiplication gain, so *EM gain is disabled* in this work (signal levels are well above the read-noise floor), which keeps CIC negligible [9].

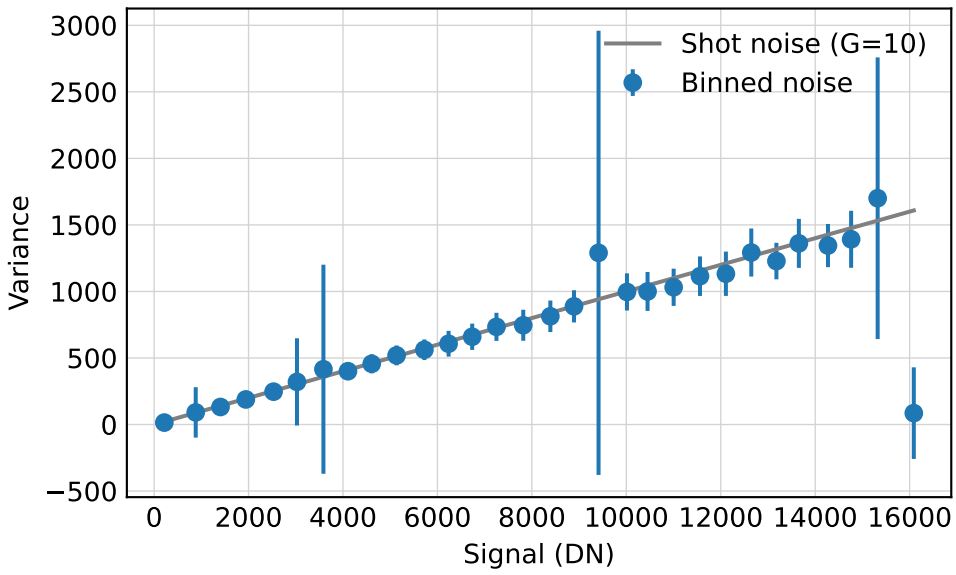


Figure 3 Measured noise vs. signal (photon-transfer curve) demonstrating shot-noise-limited operation; the linear slope yields the conversion gain G .

Shot noise and photon-transfer method. Under these optimised conditions the dominant term is shot noise. Incident photons create photoelectrons with quantum efficiency η , so $N_e = \eta N_{\text{photons}}$ and, for Poisson statistics, $\text{var}(N_e) = N_e$ [11]. Let G denote the system conversion gain (DN per electron). The measured signal in data numbers (DN) is $S = G N_e$, and the measured variance becomes $\sigma_{\text{meas}}^2 = \sigma_{\text{read}}^2 + GS$ (dark & CIC negligible, no EM gain). Thus a plot of variance vs. mean (photon-transfer curve) is linear in the shot-noise regime with slope G . Figure 3 shows this behaviour; from the slope we estimate $G \approx 10 \text{ DN}/e^-$. Note that this procedure does *not* determine η ; it only gives the DN-to-electron conversion.

Practical settings for reproducibility. (1) Keep the camera at $\leq -80^\circ\text{C}$; (2) use vertical binning to treat the EMCCD as a 1D detector; (3) disable EM gain to avoid CIC and excess-noise-factor penalties; (4) fix slit width and exposure during noise characterisation; (5) verify the shot-noise regime by measuring σ^2 vs. S and confirming linearity and slope G

4.3 Focusing and alignment

The objective is to image the excited spot on the sample onto the spectrometer fibre with maximal throughput. Parabolic mirrors (PM1/PM2) remain fixed once set; all focusing is done with the lamp, fibre/spectrometer port, and sample stages.

1. **Initial setup with a fiber coupled lamp.** Remove the sample and place a fiber-coupled lamp at the sample position. This will help align and focus the optics using visible light.
2. **Align the beam.** Adjust the lamp position and the parabolic mirrors so that the beam appears circular and sharply focused at the spectrometer fiber port. This ensures the optics are approximately aligned.

3. **Connect and optimize with spectrometer.** Connect the spectrometer to the spectrometer port and move the holder to maximize the signal roughly. Use the micrometer screws on the sample stage for fine adjustments.
4. **Swap back in the sample.** Replace the lamp with the sample at the same position. Connect the lamp output to the spectrometer port to illuminate the sample.
5. **Fine-focus the sample.** Adjust the sample position to minimize the size of the visible spot on the sample.
6. **Focus the infrared laser.** Turn on the infrared laser and use an IR detection card to locate and focus the beam onto the sample. The white light and the IR should overlap and be centered.
7. **Optimize laser alignment.** Replace the lamp with the spectrometer and monitor the reflected laser signal on the spectrometer. Fine-tune the laser focus to maximize this signal.

4.4 Data processing

All raw spectra were first corrected by subtracting a dark frame recorded with identical acquisition settings, removing the fixed electronic bias and dark current. Residual peaks at the fundamental and harmonic wavelengths of the pump laser, normally suppressed by laser line filters, were present due to the absence of suitable optical filtering. These peaks were identified and removed digitally, leaving small gaps in the plotted spectra where the affected bins were excluded.

The corrected signal $S(\lambda)$ in DN was converted to spectral power density $P_{\text{meas}}(\lambda)$ via

$$P_{\text{meas}}(\lambda) = \frac{S(\lambda)}{G t_{\text{exp}} \Delta\lambda} \frac{hc}{\lambda}, \quad (4)$$

with G the DN/ e^- conversion gain, t_{exp} the exposure time, and $\Delta\lambda$ the spectral bin width.

5 Results

The time evolution for the electron temperature $T_e(t)$ according to the ODE in [Equation 1](#) with the parameters from [Table 1](#) is shown in [Figure 4](#). A Gaussian pump drives a rapid rise of T_e followed by cooling on the electron–phonon timescale g . The shaded band indicates the propagated 1σ uncertainty; the inferred peak temperature is 8500(2500) K.

Using $T_e(t)$ as input to Planck’s law ([Equation 2](#)), the modelled spectral power density $P_{\text{model}}(\lambda)$ is computed and compared with measured spectrum in [Figure 5](#). The measured spectrum $P_{\text{measured}}(\lambda)$ is a lot lower in absolute scale than the model, therefore the measurement in [Figure 5](#) is scaled to match the model. The measured spectrum is noticeably narrower than the model, consistent with the finite sensitivity window set by the Si detector quantum efficiency and the blazed-grating envelope.

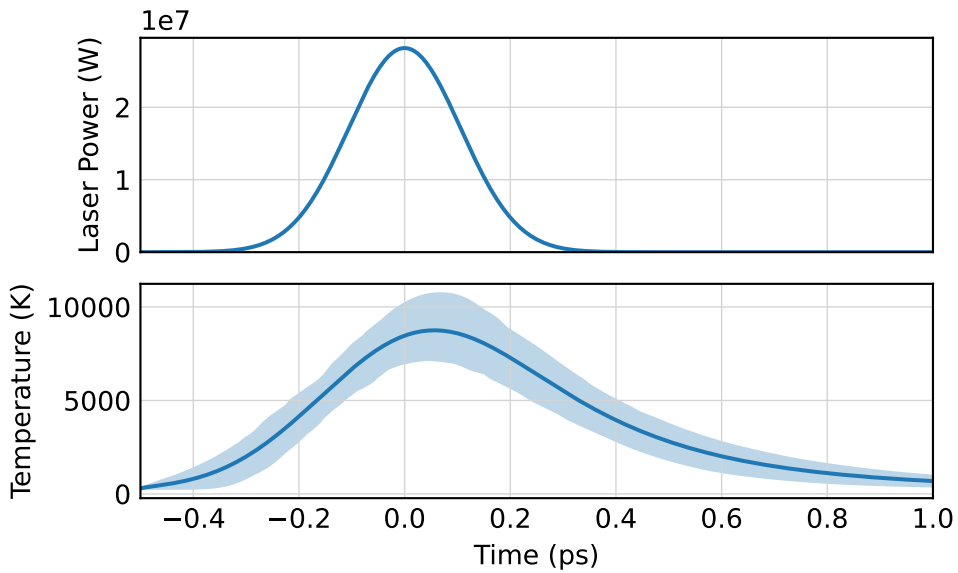


Figure 4 Gaussian pump S and computed electron temperature $T_e(t)$ from the lumped two-temperature model (parameters in Table 1). The fast rise is followed by electron–phonon cooling with time constant g . The shaded band shows the 1σ Monte Carlo uncertainty.

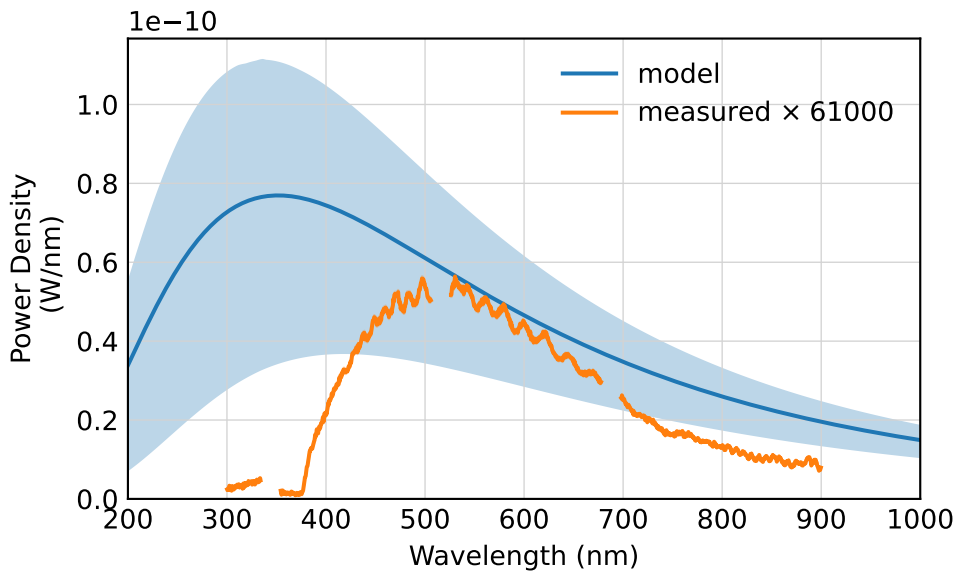


Figure 5 Measured spectral power density $P_{\text{measured}}(\lambda)$ compared with the model spectrum obtained by applying Planck's law to $T_e(t)$. The measurement is scaled to match the model. The measured peak is narrower than the model, consistent with the instrument's finite sensitivity window.

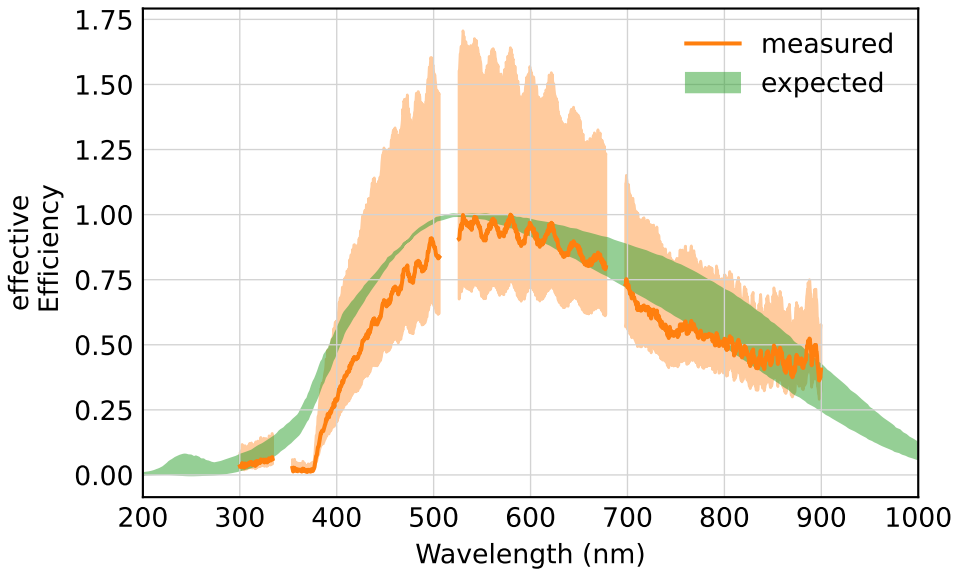


Figure 6 Effective spectrometer efficiency (peak-normalised) from $P_{\text{meas}}(\lambda)/P_{\text{model}}(\lambda)$. The overlay shows the expected relative efficiency from component specifications (camera QE \times blazed-grating model). The shaded range reflects uncertainty in blaze parameters. The measured curve shows stronger roll-off at both band edges and oscillations over wavelength.

An effective spectrometer efficiency is obtained by taking the wavelength-wise ratio

$$\eta = P_{\text{meas}}(\lambda)/P_{\text{model}}(\lambda)$$

and normalizing to its maximum, so the peak equals unity (Figure 6). The expected curve is calculated from the manufacturer’s QE data for the camera when new [12] multiplied by a blazed-grating efficiency model [13]; the shaded interval reflects uncertainty in the blaze parameters. The measured efficiency falls off more steeply than expected at both short and long wavelengths, indicating additional wavelength-dependent loss not captured by the nominal QE \times blaze model. Moreover, the measured curve exhibits oscillations over wavelength, which may indicate interference effects or ripple in the grating efficiency.

6 Discussion

The earlier-than-expected roll-off at the short-wavelength edge of the effective efficiency (Figure 6) is plausibly due to degradation of the UV-enhancing coating on the detector, consistent with the instrument’s age. The long-wavelength roll-off may stem from reduced near-IR sensitivity of the EMCCD caused by ageing-related changes in the silicon surface passivation and anti-reflection coatings, compounded by increased absorption in optical coatings and possible fibre transmission losses.

The oscillatory structure superimposed on the efficiency curve is consistent with thin-film interference effects, likely arising from oxide layers on metallic mirrors and other coated optics.

Such features are stable over short time scales but depend on the exact thickness and refractive index of the oxidised layers.

7 Conclusion

The present comparison between model and measurement is limited by the restricted sensitivity window of the existing optical path. A measurement with a calibrated, broadband setup is required to validate the model more rigorously. Furthermore, if the hot-electron emission mechanism is to be used for any serious calibration purpose, a more detailed physical model will be necessary to reduce uncertainty. Nevertheless, the principle of using hot electrons remains one of the most straightforward ways to generate broadband, predictable UV emission.

References

- [1] Howard W Yoon and Charles E Gibson. *NIST measurement services: Spectral Irradiance Calibrations*. Tech. rep. Gaithersburg, MD: National Institute of Standards and Technology, 2011. doi: [10.6028/nist.sp.250-89](https://doi.org/10.6028/nist.sp.250-89). URL: <https://nvlpubs.nist.gov/nistpubs/Legacy/SP/nistspecialpublication250-89.pdf> (visited on 07/25/2025).
- [2] V I Sapritsky. “Black-body radiometry”. en. In: *Metrologia* 32.6 (Dec. 1995), pp. 411–417. ISSN: 0026-1394, 1681-7575. doi: [10.1088/0026-1394/32/6/2](https://doi.org/10.1088/0026-1394/32/6/2). URL: <https://iopscience.iop.org/article/10.1088/0026-1394/32/6/2> (visited on 08/06/2025).
- [3] T.C. Larason, S.S. Bruce, and C.L. Cromer. “The NIST high accuracy scale for absolute spectral response from 406 nm to 920 nm”. en. In: *Journal of Research of the National Institute of Standards and Technology* 101.2 (Feb. 1996). Publisher: National Institute of Standards and Technology (NIST), p. 133. ISSN: 1044-677X. doi: [10.6028/jres.101.015](https://doi.org/10.6028/jres.101.015). URL: <https://nvlpubs.nist.gov/nistpubs/jres/101/2/j21ara.pdf> (visited on 07/25/2025).
- [4] Chun Hung Lui, Kin Fai Mak, Jie Shan, and Tony F. Heinz. “Ultrafast Photoluminescence from Graphene”. In: *Physical Review Letters* 105.12 (Sept. 2010). Publisher: American Physical Society, p. 127404. doi: [10.1103/PhysRevLett.105.127404](https://doi.org/10.1103/PhysRevLett.105.127404). URL: <https://link.aps.org/doi/10.1103/PhysRevLett.105.127404> (visited on 05/05/2025).
- [5] Leon Roob. “Thermal Radiation from Ultrafast Hot Electrons in Graphite”. en. Universität Konstanz, Apr. 2025.
- [6] T. Smausz, B. Kondász, T. Gera, T. Ajtai, N. Utry, M. Pintér, G. Kiss-Albert, J. Budai, Z. Bozóki, G. Szabó, and B. Hopp. “Determination of UV-visible-NIR absorption coefficient of graphite bulk using direct and indirect methods”. en. In: *Applied Physics A* 123.10 (Oct. 2017), p. 633. ISSN: 0947-8396, 1432-0630. doi: [10.1007/s00339-017-1249-y](https://doi.org/10.1007/s00339-017-1249-y). URL: [http://link.springer.com/10.1007/s00339-017-1249-y](https://link.springer.com/10.1007/s00339-017-1249-y) (visited on 08/09/2025).
- [7] A. Stange, C. Sohrt, L. X. Yang, G. Rohde, K. Janssen, P. Hein, L.-P. Oloff, K. Hanff, K. Rossnagel, and M. Bauer. “Hot electron cooling in graphite: Supercollision versus hot phonon decay”. In: *Physical Review B* 92.18 (Nov. 2015). Publisher: American Physical Society, p. 184303. doi: [10.1103/PhysRevB.92.184303](https://doi.org/10.1103/PhysRevB.92.184303). URL: <https://link.aps.org/doi/10.1103/PhysRevB.92.184303> (visited on 04/01/2025).
- [8] Takeshi Nihira and Tadao Iwata. “Temperature dependence of lattice vibrations and analysis of the specific heat of graphite”. In: *Physical Review B* 68.13 (Oct. 2003). Publisher: American Physical Society, p. 134305. doi: [10.1103/PhysRevB.68.134305](https://doi.org/10.1103/PhysRevB.68.134305). URL: <https://link.aps.org/doi/10.1103/PhysRevB.68.134305> (visited on 04/01/2025).
- [9] Andor. *Establishing Sensitivity in Scientific Cameras*.
- [10] Dr. Jo Walters. *Sensitivity and Noise of CCD, EMCCD and sCMOS Sensors*. Apr. 2023.
- [11] European Machine Vision Association. *Standard for Characterization of Image Sensors and Cameras*. Nov. 2010.

- [12] Andor. *iXonEM+ 897*.
- [13] P. K. Barker. “Ripple correction of high-dispersion IUE spectra - Blazing echelles”. en. In: *The Astronomical Journal* 89 (June 1984), p. 899. ISSN: 00046256. DOI: [10.1086/113587](https://doi.org/10.1086/113587). URL: http://adsabs.harvard.edu/cgi-bin/bib_query?1984AJ.....89..899B (visited on 04/07/2025).